# Distributed Sensor Networks Based Shallow Subsurface Imaging and Infrastructure Monitoring

Fangyu Li, Maria Valero, Yifang Cheng, Tong Bai, and WenZhan Song

***Abstract*—Distributed sensor networks can be used as passive seismic sensors to image and monitor subsurface and underground activities. Passive seismic surface-wave imaging adopts background ambient sounds from a far-field energy source. Because high frequency components decay a lot between the neighboring stations, conventional sparse sensor networks cannot image small-scale and shallow objects. In this article, we propose to use local seismic spatial autocorrelation coefficients, obtained by the combinations of independent dense sensor network measurements and pre-processed readings of its neighbor(s), to perform real-time collaborative imaging of the shallow subsurface objects. First, we derive the high-frequency spectral coefficient based shallow subsurface imaging method. Then, we apply the proposed approach to image a shallowly buried pipeline and obtain promising results. Furthermore, based on a time-lapse manner, the water leakage from the buried pipeline can also be detected using distributed computations between sensors. Comparisons and analysis of field deployments are made to validate the effectiveness and performance of the proposed method.**

***Index Terms*—Shallow subsurface imaging, high-frequency components, seismic interferometry, infrastructure.**

## I. Introduction

SHALLOW SUBSURFACE imaging is of great importance for understanding underground infrastructures, especially in civil engineering [1]–[3]. The seismic ambient noise imaging methods leverage background noises, such as traffic, railways as well as natural sources like long-distance earthquakes, as sources [4]–[6]. Utilizing the source energy, depth information is extracted from the dispersive frequency-phase velocity curves associated with the surface-wave propagation [7]. Compared with the intrusive investigation using borehole survey, passive surface wave methods have gained increasing popularity recently due to their non-intrusive nature [8].

Based on the Rayleigh wave analysis, the spatial autocorrelation (SPAC) method was proposed by Aki [9], which has been generalized in [10] and restated in [11]. The SPAC method extracts the scalar seismic velocity irrespective of the number of sources and the azimuths of the surface waves [12]. Also, SPAC methods have a higher resolution than $f-k$ methods [13]. Cho *et al.* [10] proposed to use power-special densities to obtain a higher resolution than SPAC.

To image shallow subsurface, high frequency information should be considered. As stated in [14], high frequency surface waves have short wavelength, only travel in a shallow depth, and are very sensitive to shallow infrastructures. However, because of the sparse deployment of traditional seismic arrays, high-frequency components decay a lot between the geophone stations, and cannot be used for seismic imaging. Taking advantage of the merging sensor network technique with a dense sensor array [2], [4], [7], [15]–[17], we can obtain seismic data with more adequate high frequency components for shallow subsurface imaging with an improved resolution. In [18], a deployment with the high spatial resolution was adopted for urban structure analysis thanks to the dense seismic array. Moreover, another ambient noise based method-interferometry has also been used to obtain 1D velocity model in Japan [19] and the depth of bedrock in Singapore [8].

However, current shallow subsurface imaging approaches typically involve manual collection of raw seismic data from sensors to a central server, as well as the post-processing and analysis. Thus, they do not have the capability of obtaining information in a real-time and automatic manner. Sensor network technology is a distributed approach with the ubiquitous in-situ computing and real-time processing ability [2]. Thus, distributed sensor network (DSN) based shallow subsurface imaging can be used to capture the temporal evolution processes, such as water leakage. We can implement the imaging system in a time-lapse manner, which has been widely used in monitoring velocity variations caused by underground mining [20], volcano eruptions [21], oil/gas production [22], reservoir flow [23], $CO_2$ sequestration [24], major earthquakes [25] and so on.

In this paper, we propose a shallow infrastructure imaging and monitoring technique based on cooperative seismic sensor networks, as shown in Fig. 1. High-frequency components of SPAC coefficients are extracted to specifically image shallow infrastructures. And a time-lapse continuous monitoring is implemented to detect velocity variations, such as water leaks. The contributions of our work are:

1) We propose to use high-frequency components to obtain high resolution shallow imaging results, which are promising for infrastructure mapping;

Manuscript received October 14, 2019; revised January 20, 2020; accepted February 9, 2020. Date of publication February 20, 2020; date of current version March 18, 2020. This work was supported by NSF-1663709 and Southern Company. The associate editor coordinating the review of this manuscript and approving it for publication was Prof. Pierluigi Salvo Rossi. *(Corresponding author: Fangyu Li.)*

Fangyu Li, Maria Valero, and WenZhan Song are with the Center for Cyber-Physical System, University of Georgia, Athens, GA 30602 USA (e-mail: fangyu.li@uga.edu; maria.valero@uga.edu; wsong@uga.edu).

Yifang Cheng is with the Department of Earth Sciences, University of Southern California, Los Angeles, CA 90007 USA (e-mail: chengyif@usc.edu).

Tong Bai is with the Department of Geoscience, University of Wisconsin-Madison, Madison, WI 53706 USA (e-mail: tbai4@wisc.edu).

Digital Object Identifier 10.1109/TSIPN.2020.2975349

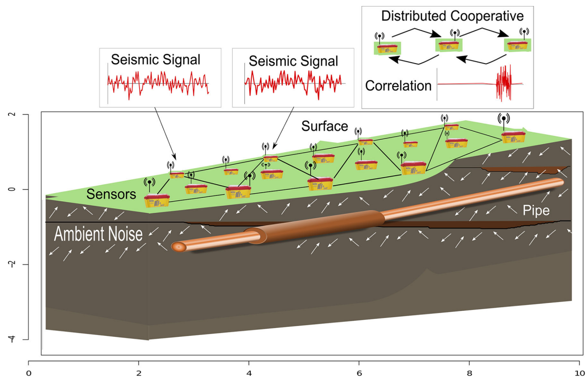


Fig. 1. Shallow infrastructure imaging based on distributed sensor networks. The surface sensor network performs the ambient noise imaging to map velocity variances caused by underground infrastructures, e.g. pipeline.

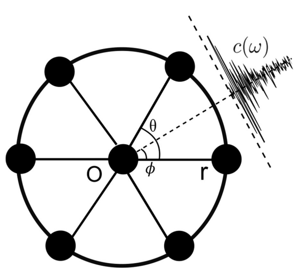


Fig. 2. A seismic surface wave propagation illustration. There is a plane wave arriving from a single direction $\phi$ at a given velocity $c(\omega)$ to a circular seismic survey.

2) A distributed algorithm for the proposed method is developed based on DSN. And a prototype system is implemented with the in-situ computation ability.
3) We propose a method (tSPAC) to continuously monitor the velocity changes caused by fluid saturation around shallow infrastructure.
4) We have accomplished field experiments of the proposed approach. We successfully imaged a shallowly buried pipeline as well as the water leakage from it, which validated the feasibility of our method and system.

The remainder of this paper is organized as follows. Section II introduces the proposed method. In Section III, we describe the detailed algorithm to implement the proposed method. Our field deployment experiment results are presented and discussed in Section IV, where both pipeline imaging and water leakage detection are included. In addition, we also discuss the controlling factors, trade-offs and related works in Sections V and VI. Finally, Section VII concludes the paper.

## II. Method

### A. Rayleigh Wave

The Rayleigh wave is assumed as a single, deterministic harmonic plane wave component which propagates from azimuth $\phi$ with angular frequency $\omega$ and absolute wavenumber $k$ [9], as shown in Fig. 2.

The contribution of the harmonic waves to the $Z$ component seismograms at location $(r, \theta)$ is obtained by correcting the phase delay and the axis rotation:

$$\begin{aligned} &Z(\omega, k, \phi; t, r, \theta) \\ &= \exp[-i\omega t - irk\cos(\phi - \theta)] h(\omega, k) \zeta'^R(\omega, k, \phi), \end{aligned} \tag{1}$$

where $\zeta'^R(\omega, k, \phi)$ denotes the complex Fourier spectra of the Rayleigh wave, and the superscript $R$ indicates the Rayleigh wave. The complex function $h(\omega, k)$ describes the amplitude ratio (reciprocal of the ellipticity) between the vertical and horizontal components of the Rayleigh waves [26].

By triply integrating the above harmonic wave components over all frequencies, wavenumbers and arrival directions, we obtain the following general representation for the vertical component $\{Z\}$ of the random field of the geophone:

$$\begin{aligned} Z(t, r, \theta) = &\int_{-\pi}^{\pi} \int_0^{\infty} \int_{-\infty}^{\infty} \exp[-i\omega t - irk\cos(\phi - \theta)] \ldots \\ &h(\omega, k) \zeta'^R(\omega, k, \phi) d\omega k dk d\phi, \\ = &\int_{-\pi}^{\pi} \int_0^{\infty} \int_{-\infty}^{\infty} \exp[-i\omega t - irk\cos(\phi - \theta)] \ldots \\ &h(\omega, k) \zeta^R(d\omega, dk, d\phi), \end{aligned} \tag{2}$$

where, $\zeta^R(d\omega, dk, d\phi)$ is an integrated spectrum, which can be expressed using the frequency-wavenumber-direction (FWD) spectral density function $F^R$ as:

$$\begin{aligned} &\langle \zeta(d\omega, dk, d\phi) \zeta^*(d\omega,' dk,' d\phi') \rangle \\ &= \delta(\omega - \omega') \left[\delta(\phi - \phi') \delta(k - k')/k\right] \\ &\quad \cdot F^R(\omega, k, \phi) d\omega d\omega' k(dkd\phi)(k'dk'd\phi') \\ &= \delta(\omega - \omega') \delta(\phi - \phi') \delta(k - k') \\ &\quad \cdot F^R(\omega, k, \phi) d\omega d\omega' k dk dk' d\phi d\phi,' \end{aligned} \tag{3}$$

where, '*' denotes the complex conjugate; $\delta(\cdot)$ stands for the Dirac function. The above expression states that the wavefield is assumed to be stationary in both time and space, which means the increments in frequency $\omega$, wavenumber $k$, and arrival direction $\phi$ of function $\zeta(d\omega, dk, d\phi)$ are mutually uncorrelated. Specifically, $\delta(\omega - \omega')$ denotes the stationarity in time, while the stationarity in space is represented by $\delta(\phi - \phi')\delta(k - k')$.

The FWD spectral density function $F^R(\omega, k, \phi)$ is defined under the assumption that the power of Rayleigh wave concentrates on discrete $N^R$ modes, which is expressed as:

$$F^R(\omega, k, \phi) = \sum_{q=1}^{N^R} f^{R(q)}(\omega, \phi) \delta(k - k^{R(q)}(\omega))/k, \tag{4}$$

where $f^R(\omega, \phi)$ is frequency-direction spectral density representing the intensity of the $(q-1)$th mode of Rayleigh wave arriving from direction $\phi$ with frequency $\omega$. Note that the wavenumber becomes a multivalued function of frequency.

### B. SPAC

Aki [9] proposed the SPAC method for surface wave imaging. Suppose there is a circular seismic sensor array as shown in Fig. 2. SPAC between the seismic wavefield obtained at a point $(r, \theta)$ on the circumference and that obtained at its center $O$ can be defined as:

$$\rho_Z(\omega, r, \theta) = \mathscr{F}\langle Z(s, r, \theta) Z^*(s - t_{\text{lag}}, 0, \theta)\rangle, \tag{5}$$

where, the vertical-motion record ($Z$ component) is defined in Eq. (2). $\mathscr{F}$ denotes the Fourier transform; '*' denotes the complex conjugate; $\langle\cdot\rangle$ stands for the ensemble mean; $s$ is the time variable and $t_{\text{lag}}$ is the time lag.

Substituting Eqs. (2), (3), and (4) into Eq. (5) yields:

$$\rho_Z(\omega, r, \theta) = \sum_{q=1}^{N^R} \int_{-\pi}^{\pi} \exp\left[-irk^{R(q)}(\omega)\cos(\phi - \theta)\right] \ldots$$
$$|h^{(q)}(\omega)|^2 f^{R(q)}(\omega, \phi) d\phi, \tag{6}$$

where the function $h(\omega, k^{(q)}(\omega))$ has been rewritten as $h^{(q)}(\omega)$ for the sake of simplicity.

The azimuthally averaged spatial autocorrelation coefficient $\bar{\rho}_{Z0}(\omega, r)$ which is the azimuthal average $\bar{\rho}_Z(\omega, r)$ of the spatial autocorrelation function $\rho_Z(\omega, r)$ normalized by the central value $\bar{\rho}_Z(\omega, 0)$, is defined as:

$$\bar{\rho}_{Z0}(\omega, r) = \frac{\bar{\rho}_Z(\omega, r)}{\bar{\rho}_Z(\omega, 0)}, \tag{7}$$

$$\bar{\rho}_Z(\omega, r) = \frac{1}{2\pi} \int_{-\pi}^{\pi} \rho_Z(\omega, r, \theta). \tag{8}$$

By substituting Eq. (6) and Eq. (8) into Eq. (7) and using the relation in Eq. (9):

$$\int_{-\pi}^{\pi} \exp[-irk\cos(\phi - \theta) - im\theta] d\theta$$
$$= 2\pi J_m(rk) \exp[-im(\phi + \pi/2)], \tag{9}$$

we have

$$\bar{\rho}_{Z0}(\omega, r) = \sum_{q=1}^{N^R} J_0\left(rk^{R(q)}(\omega)\right) \alpha^{(q)}(\omega), \tag{10}$$

where $J_m(\cdot)$ denotes the Bessel function of the first kind of order $m$, and

$$\alpha^{(q)}(\omega) = \frac{|h^{(q)}(\omega)|^2 \int_{-\pi}^{\pi} f^{R(q)}(\omega, \phi) d\phi}{\sum_{q=1}^{N^R} |h^{(q)}(\omega)|^2 \int_{-\pi}^{\pi} f^{R(q)}(\omega, \phi) d\phi}. \tag{11}$$

is the power partition ratio of the $(q-1)$th mode to the total power of the Rayleigh waves in vertical motion, and satisfies the following relationship:

$$\sum_{q=1}^{N^R} \alpha^{(q)}(\omega) = 1. \tag{12}$$

It is possible to estimate the value of the argument $rk^{R(q)(\omega)}$ by the Eq. (10), because the azimuthally averaged spatial autocorrelation coefficient $\bar{\rho}_{Z0}(\omega, r)$ can be estimated from circular array measurement records. Of special interest here is the case where only the fundamental mode of Rayleigh waves dominates ($N^R = 1$). In this case, the value of $rk^R(\omega)$ can be estimated by simply inverting the function $J_0(\cdot)$ using the observed value of $\bar{\rho}_{Z0}(\omega, r)$. One can subsequently estimate the wavenumber $k^R(\omega)$ since the array radius $r$ is known, and finally the phase velocity by $c^R(\omega) = \frac{\omega}{k^R(\omega)}$, whose details are available in Section II-D.

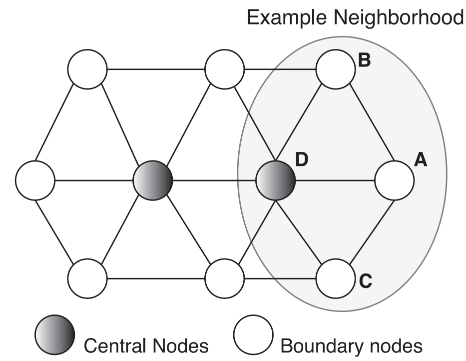


Fig. 3. Weighted SPAC coefficient estimation. A weight is assigned to each node to leverage the spatial correlation density. For example, in the annotated example neighborhood, Nodes A, B and C are boundary nodes with 3 connections, while Node D is a sink node with 6 connections. So in the SPAC coefficient estimation, Node D should have a larger weight.

As a special case, if the fundamental mode dominates the Rayleigh wave wavefield, Eq. (10) can be simplified to:

$$\bar{\rho}_{Z0}(\omega, r) = J_0\left(rk^R(\omega)\right), \tag{13}$$

where $k^R$ stands for the wavenumber of the predominant mode Rayleigh waves. And since in this situation $(N^R = 1)$, $\alpha^{(1)}(\omega) = 1$, which has been omitted.

### C. Weighted SPAC

In the general case, where the dominance of a single mode cannot be assumed, we have two unknowns for each mode, namely $k^{R(q)}(\omega)$ and $\alpha^{(q)}(\omega)(q = 1, \ldots, N^R)$. Aki proposed deploying arrays of $(N_r \geq 2\ N^R - 1)$ different radii [9], setting up the observation Eq. (10) for each radius and solving them simultaneously with the compatibility condition in Eq. (12). In the least-squares sense, SPAC coefficients can be obtained in a generalized way:

$$\min \sum_{i=1}^{N_r} \left[\bar{\rho}_{Z0}(\omega, r_i) - \sum_{q=1}^{N^R} J_0\left(r_i k^{R(q)}(\omega)\right) \alpha^{(q)}(\omega)\right]^2$$
$$\text{s.t.} \quad \text{Eq. } (12). \tag{14}$$

In Eq. (14), data from sensors located in the same radius are treated equally. However, we need also to consider the spatial confidence level of the sensor location in the shallow subsurface imaging network. As shown in Fig. 3, the confidence level of one sensor depends on the number of its neighboring nodes. For example, the "central" nodes have higher spatial correlation densities, which mean the cross-correlation pair number over the whole network denoting the sensor location, and should be given higher confidences in the SPAC coefficient estimation; while, the nodes on the boundaries would have lower spatial correlation densities, and smaller weights.

Thus, we can further develop a weighted SPAC estimation expression of the same radius $r_i$ with $M_i$ sensors:

$$\min \sum_{i=1}^{N_r} \sum_{m^i=1}^{M} \left[ \bar{\rho}_{Z0}(\omega, r_i) - \sum_{q=1}^{N^R} w_{m^i} J_0 \left( r_i k^{R(q)}(\omega) \right) \alpha^{(q)}(\omega) \right]^2, \tag{15}$$

where $w_{m^i}$ denotes the weight of $m$th sensor with the same radius $r_i$, which is estimated based on the spatial correlation density in the network.

### D. Phase Velocity Estimation

Generally, the estimation of near surface velocity profiles is based on SPAC coefficients [27]. Then the body wave velocity structure can be obtained by the inversion of the dispersion data. SPAC coefficients can be viewed as a function of inter-station distance $r$. And the phase velocities can be extracted by finding the best fit between the observed and the theoretical SPAC coefficients. In [28], a frequency dependent weight factor $A(\omega)$ was added to balance the difference in the normalization. As a result, phase velocity $c(\omega)$ can be estimated by a grid search to minimize [29]:

$$\begin{aligned} \underset{\theta}{\operatorname{argmin}} f(x) &= \text{Misfit}(\omega_i, A_i, c_k) \\ &= \text{RMS}\left( \rho(r, \omega_i) - A_i J_0 \left( r_i k^{R(q)}(\omega) \right) \right), \end{aligned} \tag{16}$$

where $\rho$ is a general SPAC coefficient, and RMS$(\cdot)$ denotes the root mean square function.

Specifically, the phase velocities are estimated by fitting the observed SPAC coefficients to the Bessel function. Based on Eq. (13), one of the variables of the Bessel function is the wave number $k = \frac{2\pi}{\lambda} = \frac{2\pi\omega}{c}$. This means, the coefficient of SPAC is related to the seismic phase velocity through the Bessel function of the first kind of order zero:

$$\rho(r, \omega) = J_0 \left[ \frac{2\pi\omega r}{c(\omega)} \right], \tag{17}$$

where $c(\omega)$ is the velocity at frequency $\omega$. The curve of SPAC coefficients is fitted to the Bessel equation in order to obtain the argument for the Bessel function $x^B$ which is correlated with the value of $2\pi\omega r$. Therefore for each argument of Bessel function $x_i^B$ we can find phase velocity at frequency $\omega_i$,

$$c(\omega_i) = 2\pi\omega r / x_i^B. \tag{18}$$

Fig. 4 shows an example of calculated SPAC coefficients and the corresponding velocity estimation [30].

To sum up, the SPAC coefficient calculation and phase velocity estimation are both constrained by the frequency range. As stated before, the imaging resolution and sensitive depth range correspond to the wave properties, which are directly related to the frequency component selection. Thus, we can select the specific frequency range to image certain objects at a given depth.

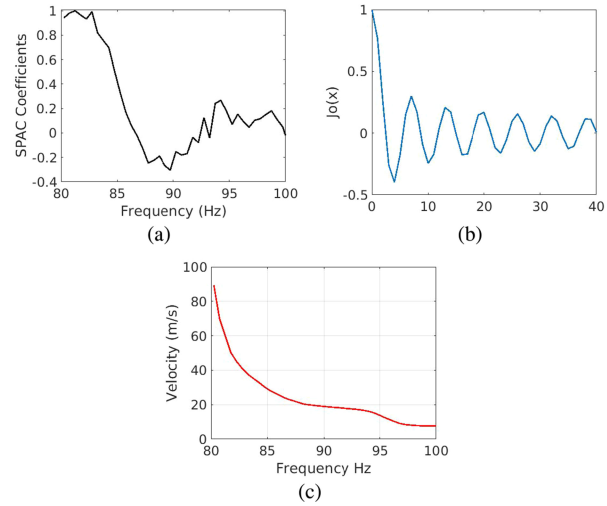


Fig. 4. (a) SPAC coefficients. (b) Bessel function of order zero. (c) Phase Velocities. [30]

### E. Time-Lapse Imaging

To achieve the time-lapse imaging, we modify the SPAC function in Eq. (5) to a tSPAC version:

$$\rho_{\text{tSPAC}}(t) = \mathcal{T}(\rho_{\text{SPAC}}) = \mathcal{T}\left( \text{SPAC}\left\{ u(t) \Big|_{t-\frac{1}{2}\Delta\tau}^{t+\frac{1}{2}\Delta\tau} \right\} \right), t \in \mathbb{R}^+, \tag{19}$$

where $\Delta\tau$ is the analysis window size, $\mathcal{T}(\cdot)$ is an online processing function, while SPAC$\{\cdot\}$ denotes the SPAC calculation within an analysis window. As an online technique, $\rho_{\text{tSPAC}}(t)$ is calculated and updated using recorded waveform from the streaming sensor. Note that because we mainly discuss the time-lapse imaging here, the sensor measurement is written as $u(t)$, and location $(r, \theta)$ is not specified.

### F. Local Normalization

To deal with the issue of unbalanced waveform amplitudes, we design a local normalization operator with a sliding-window:

$$\bar{u}(t) = \frac{u(t)}{\max\left[ |u(t - \Delta\tau/2 : t + \Delta\tau/2)| \right]}. \tag{20}$$

This operator normalizes the recorded data by the maximum absolute value in a local window centered around the time $t$.

## III. Distributed Imaging Algorithm

To acquire in-situ shallow subsurface imaging, we implement the proposed approach on DSN [4], [7]. In our system, every node reads data continuously and starts the *in-situ signal processing process*. The analysis window size is configurable in the system. Every node individually executes the data preparation, after which signals are compressed to a suitable size and transmitted in the network to improve the communication cost and

**Algorithm 1:** Distributed Shallow Subsurface Imaging and Monitoring.

1: **Input**: Size of correlation-window $t$
2: **Input**: Total size of correlation $T$
3: **Input**: Station location $x_i$, radius $r$, station number $i$
4: **While** During the deployment period
5: **While** Correlation time $T$ **do**
6: Prepare data $\mathcal{Z}_i(t)$ of size $t$
7: **For** each node $j$ in the ring of $i$ & $j$ is available
8: Receive $\mathcal{Z}_j(t)$ from node $j$
9: Correlate $\mathcal{Z}_i(t)$ and $\mathcal{Z}_j(t)$ to get the coefficient $CC_{ij}$
10: Stack correlation $CC_{ij}$ between nodes $i$ and $j$ over $T$
11: **End For**
12: **End While**
13: Calculate SPAC coefficient $\rho(r, \omega)$ for each frequency $\omega$
14: Select target frequency range
15: Estimate velocities by fitting Eq. (14).
16: Broadcast 1D velocity vector
17: **For** each sink sensor
18: Receive velocity 1D vector from every sink sensor
19: **End For**
20: Invert the phase velocity to shear wave velocity and generate the velocity structure
21: **Output**: velocity structure
22: **End While**
23: **Output**: Time-lapse velocity model

meet the bandwidth limitations. We use *zlib* data compression algorithm [31] and achieve a compression rate of $\sim$50%. A distributed algorithm is proposed and described in detail in Algorithm 1, which is based on a sink node (node located at the center of each ring) perspective. Other nodes in the ring just gather data, prepare the data for transmission, compress and broadcast the data to sink sensors. Note that this process is performed in parallel for all rings and sink nodes in the network. We use User Datagram Protocol (UDP) for broadcasting the data. In the first part of the algorithm (lines from 5 to 12), the sink sensor $i$ prepares its own data and correlate with the data that come from the nodes in its ring (nodes $j$). Note that to further diminish the communication cost, nodes can transfer just the frequency range of interest. Then, the sink node stacks the result of the window $t$ with the result $t-1$. Stacking over increasingly long time-series, on average, improves the signal-to-noise ratio. The aforementioned procedure is performed during a time $T$ (configured in the system) in which many windows of time $t$ are correlated and stacked. For instance, we can perform the cross-correlation in windows of size $t = 5$ minutes, and continue doing that for $T = 10$ hours.

In the second part of Algorithm 1 (lines from 13 to 15), the SPAC coefficients are calculated by using the average of the correlations as defined in Eq. (14). Then, the phase velocities are estimated by fitting the observed SPAC coefficients to the Bessel function. Here, sink sensors calculate velocity for the selected frequency range. The velocity estimation leads to a 1D vector that is considered as the 1D subsurface image. The subsurface imaging is performed by all sink sensors at each ring. To estimate a 3D map, sink nodes perform the third part of the algorithm (lines from 16 to 21).

In this third part, sink sensors at each ring broadcast the velocity information to the other sink nodes, and they perform an interpolation process to form a subsurface map with all the frequencies in consideration. Each layer represents a subsurface depth. With this information, we can analyze the velocity variations and determine the presence of subsurface structures within the subsurface. Besides, based on Eq. (19), the velocity maps estimated from different time can be combined together to generate a time-lapse velocity map for characterizing the temporal velocity variations.

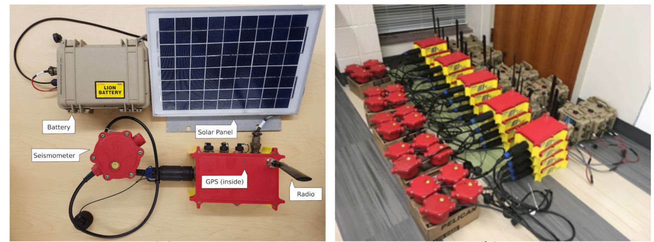


(a) (b)

Fig. 5. (a) Hardware components. (b) Seismograph nodes (for space reasons we omitted solar panels in this picture).

## IV. Experiments

### A. Prototype System

A prototype instrument to implement the proposed algorithm is shown in Fig. 5. It has geophone, GPS (global positioning system), computing board, wireless radio, solar panel and battery. Each sensor node is equipped with a wireless radio to self-form a network for communication and data exchanges. The GPS provides precise time stamp and location information for each node. The computing board inside is Raspberry Pi 3 [32], which has 1.2 GHz CPU, 1 GB RAM and GPU for intensive local computing when needed. The main components are inside a water-proof box for protecting them from harsh environment. Our seismic sensors devices were designed and developed to be computation-enabled and energy-efficient.

### B. Field Deployment 1: Pipeline Imaging

We deployed the prototype of the proposed system on the campus of the University of Georgia (UGA). This particular area has an underground metal water transportation pipeline. The area and a visual part of the pipeline are shown in Fig. 6, which is provided by the UGA Facilities Management Division, so this map can be treated as a ground truth for the validation purpose. We implemented the proposed shallow subsurface imaging method in a wireless network system, whose parameters for this experiment are listed in Table I.

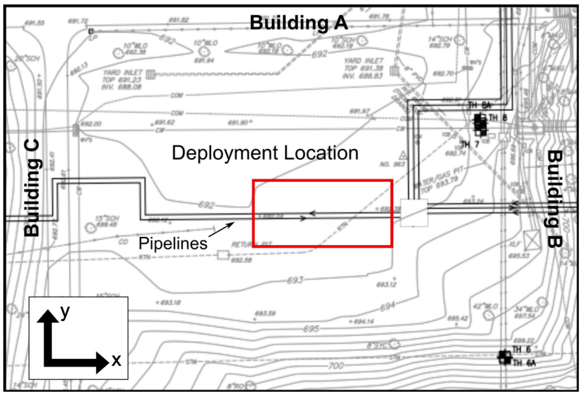


Fig. 6. Pipeline map at UGA campus, provided by the UGA Facilities Management Division. Red frame indicates the deployment location and the target pipeline.

TABLE I
DEPLOYMENT PARAMETERS USED IN UGA EXPERIMENT

| Parameter | Used Value |
|---|---|
| Number of sensors | 13 |
| Number of sink sensor | 7 |
| Radius ($r$) | Internal circle: 1.7 meters<br>External circle: 3 meters |
| Frequency range ($\omega$) | 20 Hz to 110 Hz |
| Cross-correlation window ($t$) | 5 minutes |
| Total time system running ($T$) | 4 hours |

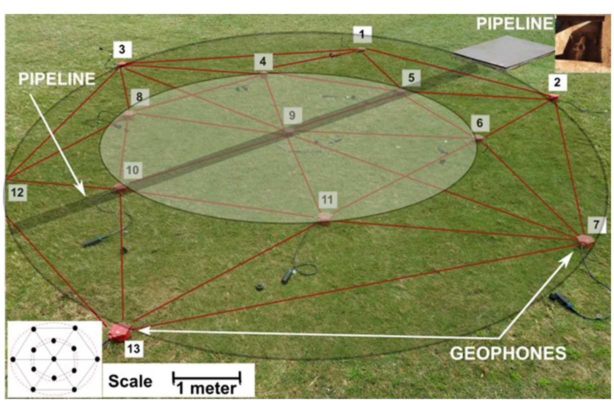


Fig. 7. Deployment location at UGA campus. Upper right: A visual of the pipeline that is with a depth around 1.6 meters. Pipeline structure is under the deployment location. The thirteen sensor nodes form two main ring with radii $r_1$ and $r_2$. Notice other sub-rings can be formed inside the main rings.

Using a mesh network, we use wireless communication and in-situ computation to generate almost real-time subsurface velocity images. Due to default SPAC method configuration, the mesh configuration is a circular array, shown in Fig. 7. The target underground pipeline is located under the surface at an approximate depth between 1.5 and 1.8 meters. Thirteen (13) seismic nodes were used for this test, and they formed a seismic mesh network for communication and collaboration. The approximate distance between sensor was 3 meters; they were located over the pipeline area. The instruments were placed in the

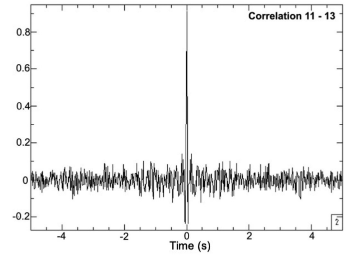


Fig. 8. Cross-correlation between pair of stations (Station 11 and Station 13 in Fig. 7).

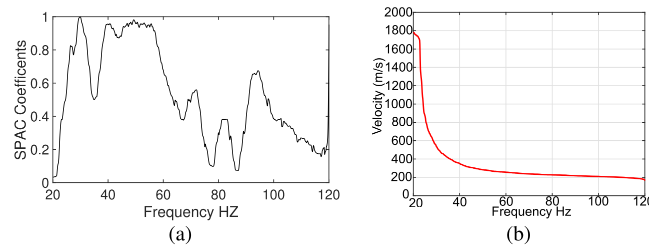


Fig. 9. (a) SPAC coefficients. (b) Velocity obtained from SPAC.

field in a ring-based topology as shown in Fig. 7. For illustration purposes, we only shows the geophone locations (without other instruments) and two rings illustration. The instruments must be placed over the structure to locate, for example a pipeline or tunnel.

Once the battery is connected to the sensors, the system automatically calibrates itself and finds GPS signal for synchronization. The system parameters are read from configuration files and the sensor reading from the medium starts. Human intervention is minimal, but the system is completely monitorable using a laptop connected to the mesh network.

The system allows the configuration of the analysis frequency range (configuration file), which incorporates flexibility to the approach. Fig. 8 shows another cross-correlation result after stacking seven hours of cross-correlation. The cross-correlation results were obtained and stacked every 5 minutes. After $T$ hours of continuous system execution, SPAC coefficients will be estimated based on the cross-correlation calculation. Then, based on the depth sensitivity kernel theory [33], shear wave velocity is inverted in the sink sensor.

Fig. 8 shows the cross-correlation coefficients calculated between two sensors. Based on the cross-correlation, we can estimate the SPAC coefficients, as shown in Fig. 9(a). Because we have not applied any spectral constraints, the SPAC coefficients span from 20 Hz to 120 Hz. Based on Eq. (16), a velocity curve can be inverted, as shown in Fig. 9(b). However, using all available frequencies is not a good strategy, because the target object corresponds to a specific narrow frequency range, while the low-frequency components corresponding to the background have stronger energies, resulting in that the target velocity variance information might be overlooked.

According to the peaks and troughs on the SPAC coefficients shown in Fig. 9(a), we first separate the entire frequency band into sub-bands: 20 to 35 Hz, 35 to 65 Hz, 65 to 77 Hz, 77 to

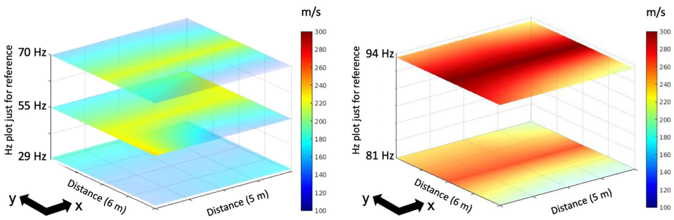


Fig. 10. Velocity maps of the spectral components with central frequencies of 29 Hz, 55 Hz, 70 Hz, 81 Hz and 94 Hz, respectively. (The axes follow the direction definition in Fig. 6.)

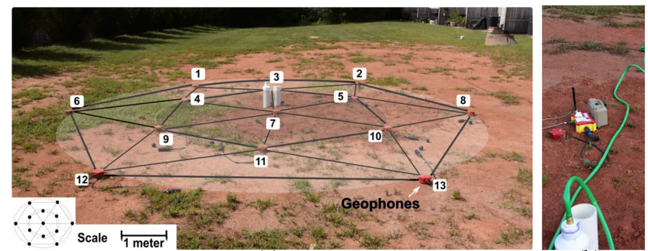


(a) (b)

Fig. 11. Deployment location at Watkinsville, GA. (a) The thirteen sensors form a circular seismic survey. For illustration purposes, we only show the geophones. (b) Injection of water into the pipeline via a hose.

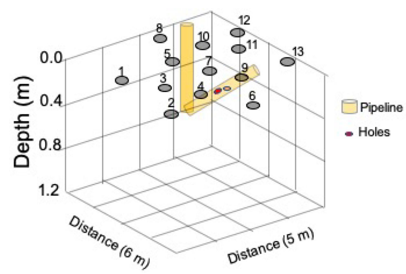


Fig. 12. Schematic map of buried pipeline and the positions of the holes for water leakage.

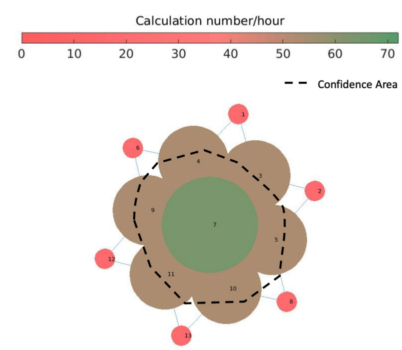


Fig. 13. Confidence map of the SPAC survey.

85 Hz, 85 to 110 Hz. Fig. 10 shows velocity maps extracted from central frequencies of 29 Hz, 55 Hz, 70 Hz, 81 Hz, and 94 Hz, respectively. As the layered half-space model defined in [34], cutoff frequencies of the fundamental mode can be expressed as:

$$f_c \approx \frac{\pi}{2\pi H\sqrt{(1/\beta_1^2 - 1/\beta_2^2)}}, \tag{21}$$

where, $\beta$ is the shear wave velocity, subscripts 1 and 2 denote surface layer and lower half space, respectively. $H$ is the depth of the layered medium. For the Poisson solid, the Rayleigh wave velocity $c = \sqrt{0.8453}\beta$ [35]. Based on the velocity curve in Fig. 9(b), the rough propagation depths of different frequency components can be obtained: 5.02 m (29 Hz), 2.65 m (55 Hz), 2.08 m (70 Hz), 1.80 m (81 Hz), and 1.55 m (94 Hz), respectively. Note that latter two components have a good correspondence with the target object.

Fig. 10 shows the imaging results of different spectral components. Note that even in the low frequency as 55 Hz, we can still observe a pipeline shape area with relatively high velocity compared to its surrounding area. However, in the upper right corner, there is a high velocity anomaly, resulting in a bad illustration of the pipeline. Considering the relationship between frequency and depth, we infer that the high velocity anomaly should locate a deeper place than the pipeline, but the imaging results are deteriorated by the poor resolution of the low-frequency components which incorporate more depths besides the target one. The pipeline is clearly imaged using the frequency range with a 94 Hz central frequency which shows a good match with the map in Fig. 6. Although the upper part has been distorted to the upper right corner, as we have seen in other frequency components, this result has shown what we expect that high frequency components can highlight velocity variance caused by infrastructure in the shallow subsurface and get rid of interferences from deeper layers.

### C. Field Deployment 2: Water Leakage Monitoring

We deployed the prototype of the proposed system at Watkinsville, GA, as shown in Fig. 11. The target underground pipeline is located under the surface at an approximate depth 0.5 m, as the schematic map with the sensor networks is shown in Fig. 12. Thirteen seismic nodes were used, and they formed a seismic mesh network for communication and collaboration. Due to SPAC constraints regarding the distance between sensor nodes, the mesh configuration must be a circular array. The approximate distance between adjacent sensors was 3 meters; they were located over the buried pipeline area. For illustration purposes, we only shows the geophone locations (without other instruments) in Fig. 11(a). Note that the instruments should be placed over the infrastructure for the monitoring purpose.

The deployment has three stages: first, we calculate the velocity model of the dry soil without pipe buried; second, after we buried the pipe, the near surface velocity was calculated; third, we use the hose on the pipe, as shown in Fig. 11(b), to inject water, after which the water leaked through the holes. We apply the tSPAC to monitor the velocity variations over the time. The whole deployment lasted for 4 hours.

Based on the survey design shown in Fig. 11(a), there are multiple ways to construct correlation pairs. Thus, the correlation calculation density is different for different nodes, resulting in different imaging confidence. We show the number of correlation pairs in Fig. 13. The survey center has the largest

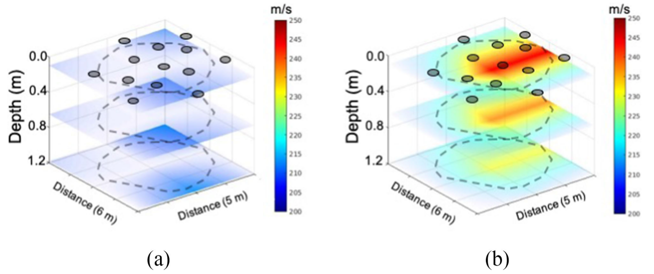


Fig. 14. (a) Velocity structure without pipelines. (b) Velocity structure with buried pipelines.

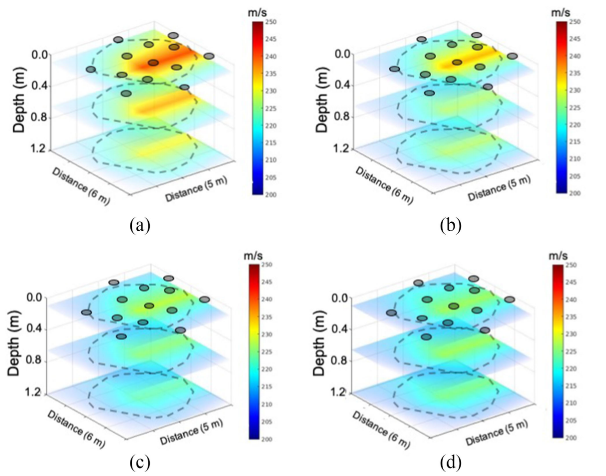


Fig. 15. Velocity structures after (a) one hour, (b) two hours, (c) three hours, and (d) four hours of water leakage.

correlation density, so the confidence is the highest, and so forth the boundaries of the survey have lower confidences. According to the largest correlation pair number, we use 80% of the peak pair number as a threshold to circle out a confident area. The dished line in Fig. 13 is the 80% confidence contour, which is also marked in the following figures.

### D. tSPAC Based Water Leakage Monitoring

Based on the selected frequency range, we can generate continuous near-surface velocity models. Fig. 14(a) shows the initial velocity before we buried the pipe, and Fig. 14(b) shows velocity model after the pipe was buried but before the water injection. The velocity was originally unformly distributed, and a velocity anomaly appeared after the pipe was buried. Subfigures in Fig. 15 display the time variant velocity models. Because of the water leakage, the velocity near the pipe location decreases with the time. Notice that, because of the hole locations in the pipe shown in Fig. 12, velocity variations are heterogeneous in all directions and areas.

Fig. 16 shows the velocity variations on different nodes. The solid curves correspond to the nodes within the confident zone, while the dishes curves show the velocity changes outside the confident zone. As we expected, in the confident zone, the velocity changes are aligned with our understandings, but in the boundary areas the velocity could vary randomly within a small range or increase because of unknown reasons.

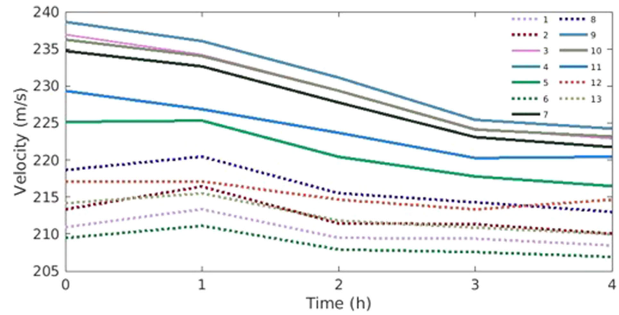


Fig. 16. Velocity changes over the 4 hours deployment at different node locations due to the water leakage.

## V. Discussions

We have evaluated the possibility of transferring the correlated raw waveform signals. However, the sensor network itself poses multiple restrictions. As we are using small sensors with limited bandwidth, transferring just short/processed information is ideal in our case. Our sensors are based on a mesh network of devices. The computational board of the device is a Raspberry Pi 3 which is chosen for its computational capabilities, bandwidth and price. In a mesh network, every hop (link) between sensors will decrease the bandwidth by half. This happens because wireless links can only do one thing at a time - transmit or receive. A long chain of mesh links results in a very slow connection from end to end. Even though this estimation (half of the bandwidth decreasing by every link) is widely accepted, in reality, other factors impact the available bandwidth in a specific time, such as, communication range, other networks interference, etc. The wireless communication bandwidth of Raspberry Pi 3 is estimated at $\sim$10 Mbps (Megabytes per second). Due to the link number in our topology (some nodes may have 5 or 6 links, which reduce the available bandwidth), we can reach a maximum available bandwidth of $\sim$2 Mbps. If we transmit correlated waveforms, our bandwidth can be severely affected and considerably reduced [4]. When we transfer only processed velocities, we save available bandwidth. So this is a trade-off that we managed by doing an acceptable interpolation based on velocities.

Another important key point of this work is the sensor network geometry. In SPAC, the array configuration plays an important role. Nodes require to be placed at the same distance from a central station. Many works have employed a circular array based on the fundamental theory of Aki [9], with one station at the centre of the circle and the other stations are on the circumference at uniform intervals, such as a seven-station "hexagonal array" [36], [37]. The hexagonal array has been used because it has the advantage of yielding independent estimates of the SPAC coefficients over radial distances simultaneously.

Additionally, a debate over the trade-off between the centralized and the decentralized approach exists. In all cases, the centralized (also called post-processing) approach generates better quality images because of no data loss. We have made an extensive comparison with post-processing approaches in our previous works [4], [7], [38]. Although the centralized image is better in comparison with decentralized results, the difference is not large enough to discard the decentralized method. And advantages of decentralized methods are significant. First, the real-time imaging is possible as there is no need of transferring data to a central place for post-processing; second, we can take advantages of the computing capabilities of the smart sensors by doing in-situ computing; and third, the network bandwidth and communication cost of the network are preserved as only a small amount of meaningful information is transferred, which avoids the communication bottlenecks. In summary, even though there is a trade-off of image quality, the advantages of the decentralized approach outperform the post-processing.

## VI. Related Work

Numerous works have been developed using active seismic and ambient noise to image subsurface structures. The major purpose of these works is to understand underground velocities for interpretation and exploration. Travel-time tomography (TT) uses the earthquake event travel time information to reconstruct a subsurface image [39]. Generally speaking, earthquake locations can be determined by inverting arrival times of body waves measured at stations of a seismic network [40]. The seismic event location accuracy is controlled by several factors, including the network geometry, available phases, arrival-time picking uncertainty [41], and accuracy of the assumed velocity model [42]. In order to improve the imaging accuracy, station and source terms can be accounted for [43], and hypocenters and velocity structure can be jointly inverted [44]. Using TT, either an active seismic source is needed or a series of local passive seismic events happen to occur at a certain time period, which are not convenient or possible, respectively. So, TT cannot be directly applied to a non-intrusive detection of underground infrastructures, like pipeline.

Extracting surface velocities, ambient noise tomography (ANT) has been widely applied worldwide (e.g. US [45], Asia [46], Europe [47], New Zealand and Australia [48].) An array of seismic stations is utilized to gather all travel time measurements together to improve the resolution of the tomographic result [49]. Besides, ANT based passive seismic monitoring has also been used for risk management and reduction in many engineering applications. For example, a hypothetical leak of $CO_2$ can be detected [50]; building properties and vulnerability for strong ground motions can be characterized [51], [52]; an active underground mine (Garpenberg, Sweden) can be monitored using ANT [53]. All these ANT-based geophysics and engineering solutions make us argue that the ambient noise can be treated as a new source that is economical, practical, and particularly valuable for seismic hazard mitigation, and abnormal activities detection in urban and non-urban areas. In fact, we have shown in this paper, that ambient noise is adequate for non-intrusive subsurface imaging of infrastructures (pipelines) and the detection of underground velocity variations that may represent a deterioration (leakages).

## VII. Conclusion

In this paper, we propose a shallow subsurface imaging technique based on DSN. The proposed method provides the opportunity to image shallow infrastructures using passive seismic waves. The principle of the proposed subsurface imaging and monitoring is to highlight the velocity variations caused by pipeline and the fluid leakage in the soil. The field deployments validate our technique, and the comparison with results from the different frequency components highlights the advantages of using high-frequency information. In addition, according to the water leakage detection experiment, our system generates a promising time-lapse velocity model. Combining the imaged pipe and velocity-reduction area, we can even further infer the water leakage location.

## References


[1] W. J. Stephenson, S. Hartzell, A. D. Frankel, M. Asten, D. L. Carver, and W. Y. Kim, “Site characterization for urban seismic hazards in lower Manhattan, New York City, from microtremor array analysis,” *Geophysical Res. Lett.*, vol. 36, no. 3, 2009, Art. no. L03301. doi: 10.1029/2008GL036444.

[2] W. Song, F. Li, M. Valero, and L. Zhao, “Toward creating a subsurface camera,” *Sensors*, vol. 19, no. 2, 2019, Art. no. 301. [Online]. Available: http://www.mdpi.com/1424-8220/19/2/301

[3] S. Wang, F. Li, M. Valero, and W. Song, “Tracking underground moving targets with wireless seismic networks,” in *Proc. IEEE Smartcomp*, 2019, pp. 425–433.

[4] M. Valero, F. Li, S. Wang, F.-C. Lin, and W. Song, “Real-time cooperative analytics for ambient noise tomography in sensor networks,” *IEEE Trans. Signal Inf. Process. Over Netw.*, vol. 5, no. 2, pp. 375–389, Jun. 2019.

[5] M. Valero, F. Li, J. Clemente, and W. Song, “Distributed and communication-efficient spatial auto-correlation subsurface imaging in sensor networks,” *Sensors*, vol. 19, no. 11, 2019, Art. no. 2427.

[6] M. Valero, F. Li, and W. Song, “Smart seismic network for shallow subsurface imaging and infrastructure security,” *Int. J. Sensor Netw.*, vol. 31, no. 1, pp. 10–23, 2019.

[7] M. Valero, G. Kamath, J. Clemente, F.-C. Lin, Y. Xie, and W. Song, “Real-time ambient noise subsurface imaging in distributed sensor networks,” in *Proc. 3rd IEEE Int. Conf. Smart Comput.*, 2017, pp. 1–8.

[8] Y. Zhang, Y. E. Li, H. Zhang, and T. Ku, “Optimized passive seismic interferometry for bedrock detection: A Singapore case study,” in *Proc. SEG Tech. Program Expanded Abstracts, Soc. of Exploration Geophys.*, 2018, pp. 2506–2510.

[9] K. Aki, “Space and time spectra of stationary stochastic waves, with special reference to microtremors,” *Bull. Earth. Res. Inst.*, vol. 35, pp. 415–456, 1957.

[10] I. Cho, T. Tada, and Y. Shinozaki, “A new method to determine phase velocities of rayleigh waves from microseisms,” *Geophysics*, vol. 69, no. 6, pp. 1535–1551, 2004.

[11] V. C. Tsai and M. P. Moschetti, “An explicit relationship between time-domain noise correlation and spatial autocorrelation (SPAC) results,” *Geophysical J. Int.*, vol. 182, no. 1, pp. 454–460, 2010.

[12] M. W. Asten, “On bias and noise in passive seismic data from finite circular array data processed using SPAC methodsBias and noise in passive seismic data,” *Geophysics*, vol. 71, no. 6, pp. V153–V162, 2006.

[13] H. Okada and K. Suto, *The Microtremor Survey Method*. Society of Exploration Geophysicists, 2003.

[14] J. Xia, R. D. Miller, C. B. Park, and G. Tian, “Inversion of high frequency surface waves with fundamental and higher modes,” *J. Appl. Geophys.*, vol. 52, no. 1, pp. 45–57, 2003.

[15] F. Li, Y. Qin, and W. Song, “Waveform inversion-assisted distributed reverse time migration for microseismic location,” *IEEE J. Sel. Topics Appl. Earth Observations Remote Sens.*, vol. 12, no. 4, pp. 1327–1332, Apr. 2019.

[16] F. Li, T. Bai, N. Nakata, B. Lyu, and W. Song, “Efficient seismic source localization using simplified gaussian beam time reversal imaging,” in *IEEE Trans. Geosci. Remote Sens.*, pp. 1–7, 2020, doi: 10.1109/TGRS.2020.2964744.

[17] F. Li, M. Valero, Y. Cheng, and W. Song, “High-frequency time-lapse seismic spatial autocorrelation imaging shallow velocity variations,” *IEEE J. Sel. Topics Appl. Earth Observations Remote Sens.*, vol. 12, no. 12, pp. 5385–5390, Dec. 2019.

[18] C. Geiss, M. Jilge, T. Lakes, and H. Taubenböck, "Estimation of seismic vulnerability levels of urban structures with multisensor remote sensing," *IEEE J. Sel. Topics Appl. Earth Observations Remote Sens.*, vol. 9, no. 5, pp. 1913–1936, May 2016.

[19] N. Nakata, R. Snieder, T. Tsuji, K. Larner, and T. Matsuoka, "Shear wave imaging from traffic noise using seismic interferometry by cross-coherence Shear wave imaging from traffic noise," *Geophysics*, vol. 76, no. 6, pp. SA97–SA106, 2011.

[20] R. Czarny *et al.*, "3D s-wave velocity imaging of a subsurface disturbed by mining using ambient seismic noise," *Eng. Geology*, vol. 251, pp. 115–127, 2019.

[21] X. Zhang and H. Zhang, "Wavelet-based time-dependent travel time tomography method and its application in imaging the Etna volcano in italy," *J. Geophysical Res.: Solid Earth*, vol. 120, no. 10, pp. 7068–7084, 2015.

[22] A. L. Vesnaver *et al.*, "Time-lapse tomography," *Geophysics*, vol. 68, no. 3, pp. 815–823, 2003.

[23] F. Sana, F. Ravanelli, T. Y. Al-Naffouri, and I. Hoteit, "A sparse Bayesian imaging technique for efficient recovery of reservoir channels with time-lapse seismic measurements," *IEEE J. Sel. Topics Appl. Earth Observations Remote Sens.*, vol. 9, no. 6, pp. 2242–2254, Jun. 2016.

[24] D. Lumley, "4D seismic monitoring of $CO_2$ sequestration," *Leading Edge*, vol. 29, no. 2, pp. 150–155, 2010.

[25] I. Koulakov, V. Gladkov, S. El Khrepy, N. Al-Arifi, and I. H. Fathi, "Application of repeated passive source travel time tomography to reveal weak velocity changes related to the 2011 Tohoku-Oki mw 9.0 earthquake," *J. Geophysical Res.: Solid Earth*, vol. 121, no. 6, pp. 4408–4426, 2016.

[26] I. Cho, T. Tada, and Y. Shinozaki, "A generic formulation for microtremor exploration methods using three-component records from a circular array," *Geophysical J. Int.*, vol. 165, no. 1, pp. 236–258, 2006.

[27] A. H. Kocaoğlu and K. Fırtana, "Estimation of shear wave velocity profiles by the inversion of spatial autocorrelation coefficients," *J. Seismology*, vol. 15, no. 4, 2011, Art. no. 613.

[28] C. Weemstra, L. Boschi, A. Goertz, and B. Artman, "Seismic attenuation from recordings of ambient noise," *Geophysics*, vol. 78, no. 1, pp. Q1–Q14, 2013.

[29] M. Ohori, A. Nobata, and K. Wakamatsu, "A comparison of ESAC and FK methods of estimating phase velocity using arbitrarily shaped microtremor arrays," *Bull. Seismological Soc. Amer.*, vol. 92, no. 6, pp. 2323–2332, 2002.

[30] M. Valero, "Real-time in-situ ambient noise seismic imaging in sensor networks," Ph.D. dissertation, University of Georgia, Athens, GA, USA, 2019.

[31] N. Kimura and S. Latifi, "A survey on data compression in wireless sensor networks," in *Proc. IEEE Int. Conf. Inf. Technol.: Coding Comput.*, 2005, vol. 2, pp. 8–13.

[32] E. Upton, "Raspberry pi 3," [Online]. Available: https://www.raspberrypi.org/products/raspberry-pi-3-model-b/, 2016.

[33] P. Chen and E.-J. Lee, *Full-3D Seismic Waveform Inversion: Theory, Software and Practice*. Berlin, Germany: Springer, 2015.

[34] Y. Xu, J. Xia, and R. D. Miller, "Approximation to cutoffs of higher modes of rayleigh waves for a layered earth model," *Pure Appl. Geophys.*, vol. 166, no. 3, pp. 339–351, 2009.

[35] W. M. Telford, W. Telford, L. Geldart, R. E. Sheriff, and R. Sheriff, *Applied Geophysics*. Cambridge, U.K.: Cambridge Univ. Press, 1990, vol. 1.

[36] M. W. Asten, "Passive seismic methods using the microtremor wave field," *ASEG Extended Abstracts*, vol. 2004, no. 1, pp. 1–4, 2004.

[37] J. C. Roberts and M. W. Asten, "Resolving a velocity inversion at the geotechnical scale using the microtremor (passive seismic) survey method," *Exploration Geophys.*, vol. 35, no. 1, pp. 14–18, 2004.

[38] M. Valero, F. Li, X. Li, and W. Song, "Imaging subsurface civil infrastructure with smart seismic network," in *Proc. 37th IEEE Int. Perform. Comput. Commun. Conf.*, 2018, pp. 1–8.

[39] G. Kamath, L. Shi, and W.-Z. Song, "Component-Average based distributed seismic tomography in sensor networks," in *Proc. 9th IEEE Int. Conf. Distrib. Comput. Sensor Syst.*, May 2013, pp. 88–95. [Online]. Available: http://dx.doi.org/10.1109/DCOSS.2013.17

[40] C. H. Thurber and N. Rabinowitz, *Advances in Seismic Event Location*. Cambridge, U.K.: Springer, 2013, vol. 18.

[41] J. Akram and D. W. Eaton, "A review and appraisal of arrival-time picking methods for downhole microseismic dataArrival-time picking methods," *Geophysics*, vol. 81, no. 2, pp. KS71–KS91, 2016.

[42] G. L. Pavlis, "Appraising earthquake hypocenter location errors: A complete, practical approach for single-event locations," *Bull. Seismological Soc. Amer.*, vol. 76, no. 6, pp. 1699–1717, 1986.

[43] W. Spence, "Relative epicenter determination using p-wave arrival-time differences," *Bull. Seismological Soc. Amer.*, vol. 70, no. 1, pp. 171–183, 1980.

[44] E. Kissling, W. Ellsworth, D. E.-Phillips, and U. Kradolfer, "Initial reference models in local earthquake tomography," *J. Geophysical Res.: Solid Earth*, vol. 99, no. B10, pp. 19 635–19 646, 1994.

[45] G. Ekström, G. A. Abers, and S. C. Webb, "Determination of surface-wave phase velocities across USArray from noise and Aki's spectral formulation," *Geophysical Res. Lett.*, vol. 36, no. 18, 2009, Art. no. L18301, doi: 10.1029/2009GL039131.

[46] L. Fang, J. Wu, Z. Ding, and G. F. Panza, "High resolution Rayleigh wave group velocity tomography in North China from ambient seismic noise," *Geophysical J. Int.*, vol. 181, no. 2, pp. 1171–1182, 2010.

[47] A. Villasenor, Y. Yang, M. H. Ritzwoller, and J. Gallart, "Ambient noise surface wave tomography of the Iberian Peninsula: Implications for shallow seismic structure," *Geophysical Res. Lett.*, vol. 34, no. 11, 2007, Art. no. L11304, doi: 10.1029/2007GL030164.

[48] P. Arroucau, N. Rawlinson, and M. Sambridge, "New insight into cainozoic sedimentary basins and palaeozoic suture zones in Southeast Australia from ambient noise surface wave tomography," *Geophysical Res. Lett.*, vol. 37, no. 7, 2010, Art. no. L07303, doi: 10.1029/2009GL041974.

[49] F.-C. Lin, M. H. Ritzwoller, and R. Snieder, "Eikonal tomography: Surface wave tomography by phase front tracking across a regional broad-band seismic array," *Geophysical J. Int.*, vol. 177, no. 3, pp. 1091–1110, 2009.

[50] A. L. Stork, C. Allmark, A. Curtis, J.-M. Kendall, and D. J. White, "Assessing the potential to use repeated ambient noise seismic tomography to detect $CO_2$ leaks: Application to the aquistore storage site," *Int. J. Greenhouse Gas Control*, vol. 71, pp. 20–35, 2018.

[51] L. Liu, Q.-F. Chen, W. Wang, and E. Rohrbach, "Ambient noise as the new source for urban engineering seismology and earthquake engineering: A case study from beijing metropolitan area," *Earthquake Sci.*, vol. 27, no. 1, pp. 89–100, 2014.

[52] A. Mordret, H. Sun, G. A. Prieto, M. N. Toksöz, and O. Büyüköztürk, "Continuous monitoring of High-Rise buildings using seismic interferometry," *Bull. Seismological Soc. Amer.*, vol. 107, no. 6, pp. 2759–2773, 2017.

[53] G. Olivier, F. Brenguier, M. Campillo, R. Lynch, and P. Roux, "Body-wave reconstruction from ambient seismic noise correlations in an underground mine," *Geophysics*, vol. 80, no. 3, pp. KS11–KS25, 2015.